A finite-element study of the onset of vortex shedding in flow past variously shaped bodies

By C. P. JACKSON

Theoretical Physics Division, Harwell Laboratory, Didcot OX11 0RA, UK

The onset of periodic behaviour in two-dimensional laminar flow past bodies of various shapes is examined by means of finite-element simulations. The transition from steady to periodic flow is marked by a Hopf bifurcation, which we locate by solving an appropriate extended set of steady-state equations. The bodies considered are a circular cylinder, triangular prisms of various shapes, and flat plates and elliptical cylinders aligned over a range of angles to the direction of flow. Our results for the circular cylinder are in good agreement with experimental observations and with the results of time-dependent calculations.

1. Introduction

Flow of a fluid past a body is a very complicated phenomenon, which can be characterized only by means of many parameters (Batchelor 1967; Dyke 1982; Tritton 1977). The most important of these is the Reynolds number Re, which is a dimensionless measure of the relative velocity of the fluid and the body. The behaviour of such flows when Re is increased is illustrated by the flow past a circular cylinder, which is shown schematically in figure 1 (*a–e*). At very low Re the flow is laminar, steady, and does not separate from the cylinder. At Re of about 6 the flow separates from the cylinder, but is still steady and laminar. At Re of about 50 the flow becomes time-dependent with the wake oscillating periodically. At higher values of Re vortices or localized regions of high vorticity are shed alternately from either side of the cylinder and are convected downstream. As Re is increased still further more frequencies enter the spectrum of the flow velocities and ultimately the flow becomes turbulent.

The periodic flow is worthy of examination both in studying the approach to turbulence and in its own right. Periodic flow leads to oscillatory forces on the body and hence to vibrations, which can be of considerable practical importance. Such vibrations occur, for example, during flow past heat-exchanger bundles, wind flow past chimneys, and flow past marine structures.

The transition to periodic behaviour as Re is varied corresponds to a Hopf bifurcation (Marsden & McCracken 1976) where an eigenvalue of the Jacobian matrix of the flow equations crosses the imaginary axis. We have employed finite-element simulation to examine the onset of periodic flows about various body shapes. However, we have not had recourse to time-dependent simulations, but have instead made direct calculations of the eigenvalues that characterize the transition to periodic flow; most importantly, we have exploited extended systems of equations for locating Hopf bifurcations. This latter approach leads to steady-state equations whose
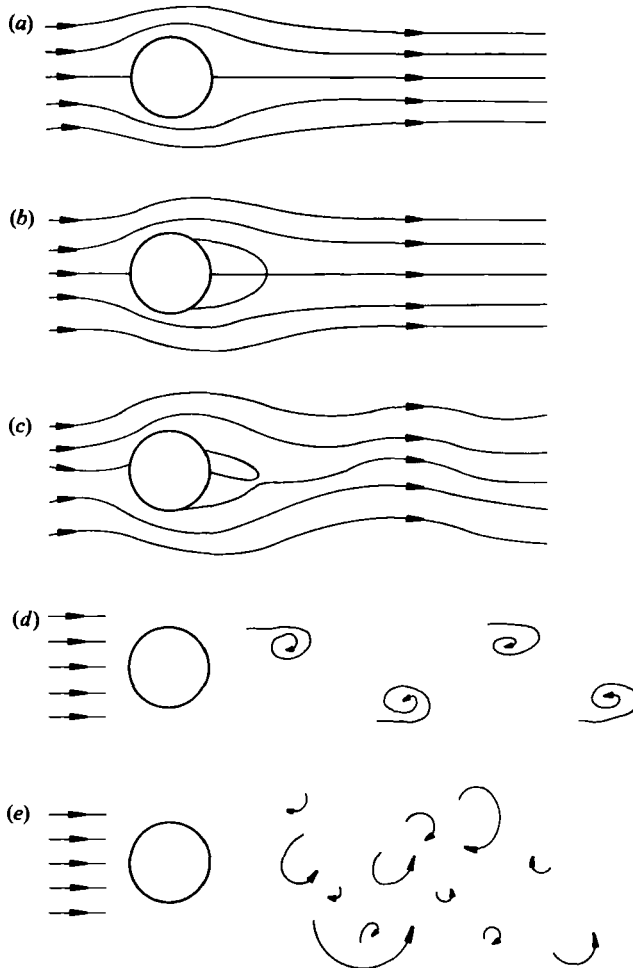
FIGURE 1. Schematic dependence on Re of the flow past a circular cylinder. (a) very low Re: no separation, (b) $6 \lesssim Re \leqslant 50$: separation, (c) $50 \lesssim Re$: periodic wake, (d) vortex shedding at Re significantly greater than 50, (e) turbulence at very large Re.

solution includes the frequency of oscillation together with the critical Re at which steady flow becomes unstable and periodic flow begins. This approach is therefore complementary to the normal method of studying oscillatory behaviour by time-dependent calculation. By solving the appropriate extended equations the actual bifurcation point can be determined extremely accurately, and the variation of the bifurcation point with other parameters can readily be studied; moreover, this approach is much cheaper than transient calculations. However, it obviously does not reveal directly how the flow changes with time.

In §2 we describe the theory that underlies our studies, including the basic flow equations, the techniques used to solve them, stability, the eigenvalue calculation and the extended system for calculating Hopf points. In §3 we describe our calculations of the onset of periodic flow about circular and elliptic cylinders, triangular prisms and flat plates. In §4 we comment upon the results and in §5 summarize the principal conclusions.

2. Theory

2.1. *Equations*

The basic equations describing laminar incompressible flow in two dimensions are the Navier–Stokes equations. These may be expressed in non-dimensional form by choosing a lengthscale L_x in the x-direction, L_y in the y-direction, a velocity scale V, and a pressure scale $P = \rho V^2$ where ρ is the density. This leads to

$$\frac{L_y}{V}\frac{\partial u}{\partial t} + \left(u\frac{1}{\Gamma}\frac{\partial u}{\partial x} + v\frac{\partial u}{\partial y}\right) + \frac{1}{\Gamma}\frac{\partial p}{\partial x} - \frac{1}{Re}\left(\frac{1}{\Gamma^2}\frac{\partial^2 u}{\partial x^2} + \frac{\partial^2 u}{\partial y^2}\right) = 0,$$

$$\frac{L_y}{V}\frac{\partial v}{\partial t} + \left(u\frac{1}{\Gamma}\frac{\partial v}{\partial x} + v\frac{\partial v}{\partial y}\right) + \frac{\partial p}{\partial y} - \frac{1}{Re}\left(\frac{1}{\Gamma^2}\frac{\partial^2 v}{\partial x^2} + \frac{\partial^2 v}{\partial y^2}\right) = 0,$$

$$\frac{1}{\Gamma}\frac{\partial u}{\partial x} + \frac{\partial v}{\partial y} = 0, \tag{1}$$

where x, y are the non-dimensional coordinates, u is the non-dimensional velocity in the x-direction, v is the non-dimensional velocity in the y-direction, Γ is the aspect ratio ($\Gamma = L_x/L_y$), Re is the Reynolds number ($Re = \rho V L_y/\mu^{\mathrm{f}}$ where μ^{f} is the fluid viscosity). Separate lengthscales were chosen deliberately for the x- and y-directions so that the aspect ratio Γ appears explicitly in the equations. Subsequently we shall vary Γ as a convenient means of distorting a circular into an elliptical body, and hence are able to follow the resulting changes in flow by a parameter-stepping technique.

2.2. *Steady-state solution and parameter stepping*

We approximate the steady-state equations derived from (1) (and also the time-dependent equations) by a standard Galerkin formulation of the finite-element method. The nonlinear equations arising from this discretization may be written in the general form

$$g(X; \lambda, \mu) = 0, \tag{2}$$

where X is the solution vector (of unknown velocities and pressures), λ is a specific parameter (Re in the present case), and μ is the vector of the remaining parameters (including Γ in this case). The nonlinear equations (2) are solved by successive Newton–Raphson iteration:

$$\mathrm{d}X^n = X^{n+1} - X^n,$$

$$g_X(X^n; \lambda, \mu)\,\mathrm{d}X^n = -g(X^n; \lambda, \mu), \tag{3}$$

where $g_X = \partial g/\partial X$ is the Jacobian matrix. These iterations continue until convergence is satisfactory. We usually converge the results to 8 significant figures. At each step a direct frontal solver is applied to the set of linear equations (3), so that g_X is decomposed into a product

$$g_X = LU, \tag{4}$$

where L and U are respectively lower and upper triangular matrices. The computation of $\mathrm{d}X^n$ by successive solution of the sets of linear equations

$$\left.\begin{array}{l} L\,\mathrm{d}Y^n = -g(X^n; \lambda, \mu), \\[2mm] U\,\mathrm{d}X^n = \mathrm{d}Y^n, \end{array}\right\} \tag{5}$$

is straightforward and incurs little expense.

The most demanding step in this procedure is the LU decomposition of g_X at each iteration; the cost is proportional to NF^2, where N is the total number of unknowns, and F is the front width of the problem. However, the LU decomposition does not involve the right-hand side of (3), so that it is then very cheap to solve for additional right-hand sides for any specific matrix. This advantage is exploited in parameter stepping as follows. The Newton–Raphson iterations converge quadratically, provided that the initial guess is close enough to the solution, but may not converge if the initial guess is not good enough. Now once the solution X_1 at one parameter value λ_1 has been found, then a very good initial guess at parameter value λ_2 can be obtained from the expression

$$X_1 + \frac{\partial X_1}{\partial \lambda}(\lambda_2 - \lambda_1). \tag{6}$$

The derivative vector $\partial X_1/\partial \lambda$ can be readily calculated since it satisfies

$$g_X \frac{\partial X_1}{\partial \lambda} = -\frac{\partial g}{\partial \lambda}; \tag{7}$$

this equation resembles (3), but with a different right-hand side. However, the Jacobian matrix g_X will have already been calculated and decomposed in order to carry out the final Newton–Raphson iteration that provided the converged solution X_1. As a result, (7) can be solved very cheaply and hence the parameter-stepping expression (6) evaluated. Thus flow solutions at a set of parameter values may be obtained much more economically by parameter stepping than by beginning each calculation from a fixed initial guess, from which iterations may well fail to converge to a solution.

2.3. *Stability*

The time-dependent discretized equations can be written as

$$M\dot{X} + g(X; \lambda, \mu) = 0, \tag{8}$$

where M is a 'mass matrix', which is of course singular in the current example. The evolution of small perturbations ε from a steady solution X_0 is described to lowest order by the linear equation

$$M\dot{\varepsilon} + g_X(X_0; \lambda, \mu)\varepsilon = 0. \tag{9}$$

If ξ is a generalized eigenvector of g_X with eigenvalue σ, such that

$$g_X \xi = \sigma M \xi, \tag{10}$$

and if ε is a perturbation along ξ, then

$$\varepsilon = \varepsilon_0\, \mathrm{e}^{-\sigma t}\, \xi, \tag{11}$$

where ϵ_0 is the component of ε along ξ at $t = 0$. Thus small perturbations about a given steady state X_0 will decay if all the generalized eigenvalues of g_X have positive real part; this criterion ensures that the steady state is stable. If, however, one or more eigenvalues have a negative real part, then the steady solution is unstable, since a perturbation along the appropriate eigenvector is unbounded (at least in the linear approximation).

As the parameter λ is varied, a steady solution may lose stability in one of two ways. The eigenvalue that gives rise to the loss of stability may cross the imaginary axis with zero imaginary part. This case corresponds either to a limit point or to a bifurcation to another steady solution. Alternatively the eigenvalue may cross the

imaginary axis at a finite imaginary value $i\omega$; this Hopf bifurcation marks a transition to a periodic solution with angular frequency ω and period $2\pi/\omega$; however, a Hopf bifurcation must also satisfy additional criteria, of which the most important is that other eigenvalues do not simultaneously cross the imaginary axis at an integral multiple of $i\omega$. For present purposes it is convenient to employ a non-dimensional measure of the frequency, that is the Strouhal number

$$St = \frac{\omega}{2\pi} \frac{L_y}{V}. \tag{12}$$

2.4. *Eigenvalue calculation*

The matrices involved in solving typical flow simulations are very large, so the LR, QR or similar algorithms for calculating eigenvalues are prohibitively expensive. Moreover, such techniques are not applicable to the general case when $\boldsymbol{g}_X$ is not symmetric and $\boldsymbol{M}$ is not the identity. Instead we have used several techniques for determining generalized eigenvalues and eigenvectors that are based on the concept of inverse iteration (Wilkinson 1965).

Inverse iteration is best illustrated by means of the generalized eigenvalue problem

$$\boldsymbol{A}\xi = \sigma\boldsymbol{B}\xi; \tag{13}$$

we shall adopt as a convenient normalization for the generalized eigenvectors ξ

$$(e^r)^{\mathrm{T}} \cdot \xi = 1, \tag{14}$$

where e^r is the unit vector with components $(e^r)_i = \delta_{ir}$. The Newton–Raphson method applied to this problem provides the iteration scheme

$$\left.\begin{array}{r}(\boldsymbol{A} - \sigma^n\boldsymbol{B})(\xi^n + \mathrm{d}\xi^n) - \mathrm{d}\sigma^n\boldsymbol{B}\xi^n = 0, \\[2mm] (e^r)^{\mathrm{T}} \cdot \mathrm{d}\xi^n = 0. \end{array}\right\} \tag{15}$$

This scheme may be realized by solving successively

$$\left.\begin{array}{c}(\boldsymbol{A} - \sigma^n\boldsymbol{B})\,\xi'^{n+1} = \boldsymbol{B}\xi^n, \\[3mm] \mathrm{d}\sigma^n = \dfrac{1}{(e^r)^{\mathrm{T}} \cdot \xi'^{n+1}}, \\[3mm] \xi^{n+1} = \xi^n + \mathrm{d}\xi^n = \dfrac{\xi'^{n+1}}{(e^r)^{\mathrm{T}} \cdot \xi'^{n+1}}. \end{array}\right\} \tag{16}$$

The first step of (16) requires an $\boldsymbol{LU}$ decomposition of $\boldsymbol{A} - \sigma^n\boldsymbol{B}$, as in §2.2. The entire procedure may be implemented by means of a simple modification to a finite-element package, which is altered so that the standard matrix-assembly routines calculate $\boldsymbol{A} - \sigma^n\boldsymbol{B}$; in our particular problem this change amounts to calculating $\boldsymbol{g}_X - \sigma^n\boldsymbol{M}$ rather than $\boldsymbol{g}_X$. If σ^n is updated according to (16), then the matrix $\boldsymbol{A} - \sigma^n\boldsymbol{B}$ becomes increasingly singular. However, it is easy to see that the matrix of the augmented system (15), which may be written

$$\begin{pmatrix} \boldsymbol{A} - \sigma^n\boldsymbol{B} & -\boldsymbol{B}\xi^n \\ (e^r)^{\mathrm{T}} & 0 \end{pmatrix} \begin{pmatrix} \mathrm{d}\xi^n \\ \mathrm{d}\sigma^n \end{pmatrix} = -\begin{pmatrix} (\boldsymbol{A} - \sigma^n\boldsymbol{B})\,\xi^n \\ 0 \end{pmatrix}, \tag{17}$$

is not singular. This latter scheme with an augmented matrix can also be implemented in a standard finite-element package, although it requires more substantial modifi-

cations to the package than does (16). The two schemes are of course equivalent in infinite-precision arithmetic, and both converge quadratically.

If σ is not updated but rather is kept fixed say at σ_0, then successive iterations of (16) or (17) are relatively cheap, since the LU decomposition of $A - \sigma_0 B$ only needs to be carried out once. This iterative scheme converges linearly to the eigenvector corresponding to the eigenvalue nearest to σ_0, but the rate of convergence may be very slow indeed if there are several eigenvalues close to σ_0. Moreover, the scheme produces only one eigenvector and eigenvalue for a particular choice of σ_0.

However, the convergence rate may be improved, and also several eigenvectors and eigenvalues determined simultaneously, by subspace iteration; that is by applying $(A - \sigma_0 B)^{-1}$ repeatedly to a set of m vectors $[\xi^1, \dots, \xi^m]$. Without loss of generality we may re-order the components of the vectors and matrices so that the 'normalization' for the set of vectors is

$$(\xi^i)_j = \begin{cases} 1, j = i, \\ 0, j < i. \end{cases} \tag{18}$$

Given any un-normalized, linearly independent set of vectors $[\xi'^i, \dots, \xi'^m]$, they can be normalized according to (18) by means of the recursion

$$\left. \begin{aligned} \xi''^i &= \xi'^i - \sum_{j < i} \xi'^j (\xi'^i)_j, \\ \xi^i &= \frac{\xi''^i}{(\xi''^i)_i}. \end{aligned} \right\} \tag{19}$$

From such a normalized set of m vectors $[\xi^1, \dots, \xi^m]$, we calculate $[\eta^1, \dots, \eta^m]$ (un-normalized) such that

$$(A - \sigma_0 B)^{-1} B [\xi^1, \dots, \xi^m] = [\eta^1, \dots, \eta^m]. \tag{20}$$

Then we define $m \times m$ matrices E and H that comprise the first m rows of $[\xi^1, \dots, \xi^m]$ and $[\eta^1, \dots, \eta^m]$ respectively, so $E_{ij} = (\xi^j)_i$ and $H_{ij} = (\eta^j)_i$. The matrix K, which is defined by

$$EK = H, \tag{21}$$

can be calculated recursively:

$$K_{ij} = H_{ij} - \sum_{k < i} E_{ik} K_{kj}, \tag{22}$$

and its eigenvalues obtained. Since K is comparatively small and an eigenvalue rather than a generalized eigenvalue is sought, any available algorithm may be used to obtain the eigenvalues of K. The sequence of steps (19)–(22) comprise one iteration of the subspace iteration algorithm, which would start again from $[\eta^1, \dots, \eta^m]$. The iterations are repeated until satisfactory convergence is achieved. Then if K has an eigenvector ζ with eigenvalue λ at convergence, it is easy to see that

$$[\xi^1, \dots, \xi^m] \zeta \tag{23}$$

is a generalized eigenvector of A with eigenvalue $\sigma_0 + (1/\lambda)$, where of course $[\xi^1, \dots, \xi^m]$ is taken from the final iteration.

Such subspace iteration yields the m generalized eigenvalues nearest to σ_0, and the corresponding generalized eigenvectors. Complex pairs may be included, but of course only those that are near to the real value σ_0. However, the techniques described can be extended so as to identify the eigenvalue or eigenvalues nearest to an arbitrary complex number σ_0; it is necessary only to work throughout with complex numbers,

or more conveniently with ordered pairs (a, b) corresponding to $a + ib$. Thus a complex generalized eigenvector $(\xi_r, \xi_i) \equiv \xi_r + i\xi_i$ with complex eigenvalue $(\sigma_r, \sigma_i) \equiv \sigma_r + i\sigma_i$ satisfies

$$\boldsymbol{A}(\xi_r + i\xi_i) = (\sigma_r + i\sigma_i)\boldsymbol{B}(\xi_r + i\xi_i); \tag{24}$$

or equivalently

$$\left. \begin{aligned} \boldsymbol{A}\xi_r &= \sigma_r \boldsymbol{B}\xi_r - \sigma_i \boldsymbol{B}\xi_i, \\ \boldsymbol{A}\xi_i &= \sigma_i \boldsymbol{B}\xi_r + \sigma_r \boldsymbol{B}\xi_i. \end{aligned} \right\} \tag{25}$$

The techniques for finding eigenvalues and eigenvectors that we have described can be readily extended so as to cope with these latter equations. However, of course, the iterative schemes involve operations with a matrix twice the size of the matrix in (16), and so the cost of the $\boldsymbol{LU}$ decomposition is eight times larger. The approach based upon complex arithmetic requires an $\boldsymbol{LU}$ decomposition that costs only four times that for the matrix in (16), but of course it is necessary to provide a complex frontal solver, and hence to make greater changes to a standard finite-element code.

2.5. *The extended system for locating a Hopf bifurcation*

At the Hopf bifurcation point a complex pair of eigenvalues with non-zero imaginary parts crosses the imaginary axis. That bifurcation is the solution of the following extended system (Griewank & Reddien 1983; Jepson 1981) of equations:

$$\left. \begin{aligned} \boldsymbol{g}(X; \lambda, \mu) = 0, \quad \boldsymbol{g}_X \xi_r + \omega \boldsymbol{M}\xi_i = 0, \quad \boldsymbol{g}_X \xi_i - \omega \boldsymbol{M}\xi_r = 0, \\ (\boldsymbol{e}^k)^{\mathrm{T}} \cdot \xi_r = 0, \quad (\boldsymbol{e}^k)^{\mathrm{T}} \cdot \xi_i = 1; \end{aligned} \right\} \tag{26}$$

we solve for the flow X, for the angular frequency ω, for the real and imaginary parts ξ_r and ξ_i of the bifurcating eigenvector, and for the critical value of one specific parameter (Re in this case), at prescribed values of all the other parameters. This extended system of equations is solved by means of Newton–Raphson linearization and a frontal solver, as described in §2.2. At first sight it might seem that this procedure leads to a matrix that is approximately three times as large as the matrix in §2.2, with a front width three times as large; hence the necessary $\boldsymbol{LU}$ decomposition might cost twenty-seven times as much as the $\boldsymbol{LU}$ decomposition for the simple flow problem. However, the extended system can in fact be solved by a much cheaper two-step process, for about one-third this cost. The Newton–Raphson linearization of (26) leads to

$$\left. \begin{aligned} \boldsymbol{g}_X \mathrm{d}X + \boldsymbol{g}_\lambda \mathrm{d}\lambda = -\boldsymbol{g}, \\ \boldsymbol{g}_{XX}\xi_r \mathrm{d}X + \boldsymbol{g}_{X\lambda}\xi_r \mathrm{d}\lambda + \boldsymbol{g}_X \mathrm{d}\xi_r + \omega \boldsymbol{M} \mathrm{d}\xi_i + \mathrm{d}\omega \boldsymbol{M}\xi_i + \omega \boldsymbol{M}_\lambda \xi_i \mathrm{d}\lambda = -(\boldsymbol{g}_X \xi_r + \omega \boldsymbol{M}\xi_i), \\ \boldsymbol{g}_{XX}\xi_i \mathrm{d}X + \boldsymbol{g}_{X\lambda}\xi_i \mathrm{d}\lambda + \boldsymbol{g}_X \mathrm{d}\xi_i - \omega \boldsymbol{M} \mathrm{d}\xi_r - \mathrm{d}\omega \boldsymbol{M}\xi_r - \omega \boldsymbol{M}_\lambda \xi_r \mathrm{d}\lambda = -(\boldsymbol{g}_x \xi_i - \omega \boldsymbol{M}\xi_r), \\ (\boldsymbol{e}^k)^{\mathrm{T}} \cdot \mathrm{d}\xi_r = 0, \\ (\boldsymbol{e}^k)^{\mathrm{T}} \cdot \mathrm{d}\xi_i = 0, \end{aligned} \right\} \tag{27}$$

where by $\boldsymbol{g}_{XX}\xi_r \mathrm{d}X$ we mean $(\partial^2 \boldsymbol{g}/\partial X_j \partial X_k)\xi_{rj}\mathrm{d}X_k$ (using the summation convention) and similarly for the other terms.

If we now evaluate

$$\boldsymbol{a} = -\boldsymbol{g}_X^{-1}\boldsymbol{g}, \quad \boldsymbol{\beta} = -\boldsymbol{g}_X^{-1}\boldsymbol{g}_\lambda, \tag{28}$$

and substitute

$$\mathrm{d}X = \boldsymbol{a} + \mathrm{d}\lambda\boldsymbol{\beta}, \tag{29}$$

into the last four equations of (27), then

$$g_X \, d\xi_r + \omega M \, d\xi_i + (g_{XX} \xi_r \beta + g_{X\lambda} \xi_r + \omega M_\lambda \xi_i) \, d\lambda + M\xi_i \, d\omega$$
$$= -(g_X \xi_r + \omega M\xi_i + g_{XX} \xi_r \, a),$$
$$g_X \, d\xi_i - \omega M \, d\xi_r + (g_{XX} \xi_i \beta + g_{X\lambda} \xi_i - \omega M_\lambda \xi_r) \, d\lambda - M\xi_r \, d\omega$$
$$= -(g_X \xi_i - \omega M\xi_r + g_{XX} \xi_i \, a), \tag{30}$$
$$(e^k)^{\mathrm{T}} \cdot d\xi_r = 0,$$
$$(e^k)^{\mathrm{T}} \cdot d\xi_i = 0.$$

These equations can be solved for $d\xi_r$, $d\xi_i$, $d\omega$ and $d\lambda$, and then finally dX can be calculated from (29). The solution of both the simple flow problem and the equations (28) requires the LU decomposition of g_X. The cost of the LU decomposition of the matrix A^* of the set of equations (30), which matrix is twice as large as g_X and has twice the front width, is approximately eight times greater. Thus the total cost of solving the extended equations (27) is about nine times that of the basic flow calculation.

Of course the extended equations (26) may be regarded as a larger system:

$$f(Y; \mu) = 0, \tag{31}$$

where
$$Y = (X, \xi_r, \xi_i, \omega, \lambda); \tag{32}$$

we may therefore parameter step for this system, varying the parameter μ.

3. Computations

3.1. *Finite elements*

We have investigated the onset of vortex shedding, that is periodic behaviour, for flow past circular and elliptical cylinders, triangular prisms and flat plates. In discussing our two-dimensional calculations, it is convenient to refer to these bodies as circles, ellipses, triangles and plates, since this is their appearance in the computational domain.

Our calculations were performed with the finite-element program TGSL (Jackson 1982), which includes all the algorithms discussed above. The velocities were interpolated by the standard nine-node biquadratic quadrilateral isoparametric element, whereas the pressure was represented by a piecewise discontinuous linear function.

In order to avoid complications with boundary conditions at infinity, a specific finite domain was defined; in terms of a scale in which one dimension of the body is one, and taking $\Gamma = 1$, this domain is defined thus:

$$-5 \leqslant x \leqslant 15, \quad -5 \leqslant y \leqslant 5, \tag{33}$$

where the x-direction is parallel to the flow. This domain is illustrated in figure 2 for a circular body, with the diameter set to one to define the lengthscale. In some sense, of course, this problem is closer to experiment than the infinite-domain problem, since most experiments are carried out in finite tanks or wind-tunnels. (We intend in
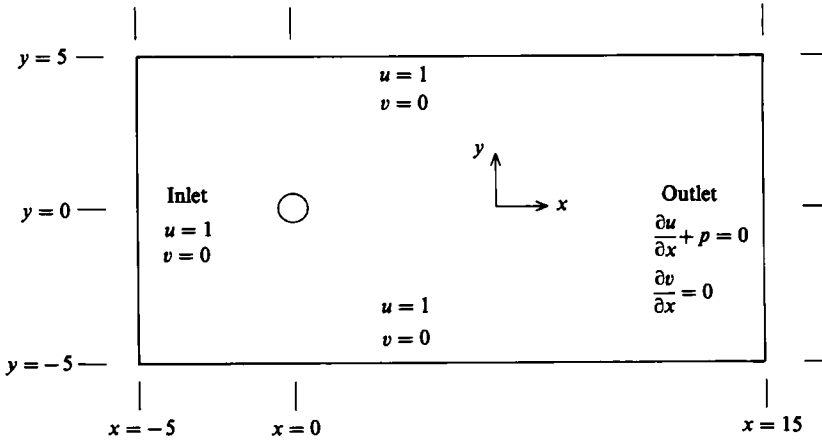
FIGURE 2. Computational domain for a circular cylinder.

subsequent work to explore the effects of domain size.) We chose boundary conditions as follows:

on the left-hand inlet and along the top and bottom of the domain

$$u = 1, \quad v = 0;$$

on the body

$$u = 0, \quad v = 0;$$

and at the outlet on the right-hand side of the domain

$$\frac{\partial u}{\partial x} + p = 0, \quad \frac{\partial v}{\partial x} = 0. \qquad \qquad (34)$$

These boundary conditions correspond more or less to 'tow tank' conditions. The outlet boundary conditions were chosen to impose as little constraint as possible on the flow calculation, to allow possible periodic flow to 'escape' from the domain.

We also made calculations for:

(i) ellipses oriented along the flow with axis $a_\parallel$ along the direction of flow and axis 1 perpendicular to the flow;

(ii) ellipses with major axis 1 and minor axis 0.5 oriented at various angles θ to the flow;

(iii) flat plates of length 1 with normal at various orientations θ to the flow; and

(iv) isosceles triangles with base 1 and height h, with apex towards the flow.

The geometry of these other body shapes is shown in figure 3. It should be noted that one dimension of the body is 1 in each case. This dimension of course corresponds to the lengthscale that was used to define the Reynolds number. We may express the Reynolds number in terms of physical dimensional quantities as follows:

(i) for an ellipse oriented along the flow, with dimensional axes $a'_\parallel$ along the flow and $a'_\perp$ perpendicular to the flow we have

$$Re = \frac{\rho V a'_\perp}{\mu^f};$$

(ii) for an ellipse with dimensional major axis a'_{maj} and minor axis a'_{min} ($= 0.5 a'_{maj}$) with the minor axis oriented at an angle θ to the flow we have

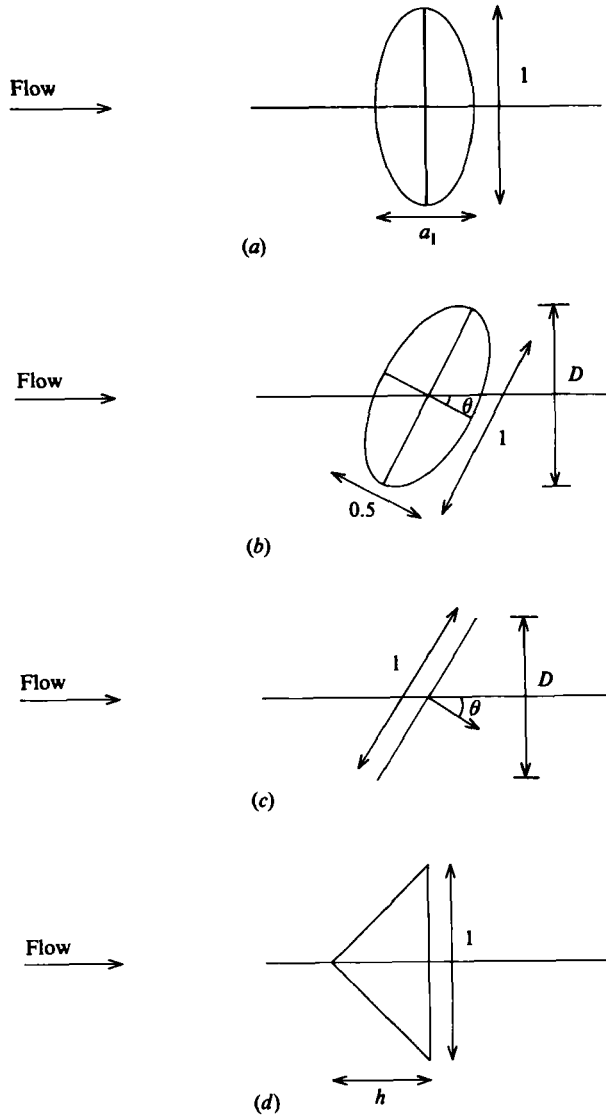$$Re = \frac{\rho V a'_{maj}}{\mu^f};$$

FIGURE 3. Geometry of the various bodies considered: (*a*) ellipse oriented along the flow, (*b*) ellipse oriented at an angle to the flow, (*c*) flat plate oriented at an angle to the flow (*d*) isosceles triangle oriented symmetrically about the flow.

(iii) for a flat plate of dimensional length L' with normal at an angle θ to the flow we have

$$Re = \frac{\rho V L'}{\mu^f};$$

(iv) for an isosceles triangle with dimensional base b' and height h' we have

$$Re = \frac{\rho V b'}{\mu^f};$$

where V is of course the velocity relative to the body of the fluid at infinity. In the case of the ellipse and flat plate oriented at an angle to the flow we also define a

Reynolds number Re^D based on the length D presented by the body normal to the flow. For the ellipse we have

$$Re^D = Re\,\cos\theta\left(1 + \left(\frac{a_{\min}}{a_{\text{maj}}}\right)^2 \tan^2\theta\right)^{\frac{1}{2}},$$

where a_{maj} and $a_{\min}$ are respectively the major and minor axis of the ellipse; and for the flat plate we have

$$Re^D = Re\,\cos\theta.$$

The basic finite-element grid used for studying the flow past a circular body is shown in figure 4. This grid has 736 elements, 3056 nodes and 8320 degrees of freedom for the velocities and pressure. The grids used for the other body shapes were obtained by a suitable mapping of this grid. For example, figure 5 shows a detail of the grid used to study flow past an ellipse with major and minor axes 1 and 0.5 respectively, with the ellipse oriented at an angle of 60° to the flow.

The calculation for the circular body was repeated on a finer grid in order to check the grid dependence of the results. A very fine grid was obtained by subdividing each element of the original grid into two in each direction, and comprised 2944 elements, 12000 nodes, and 32832 freedoms.

3.2. *Computational procedure*

The algorithm for locating a Hopf bifurcation will converge only from a very good initial guess for the basic flow, the critical Reynolds number Re_c, the critical Strouhal number St_c, and most importantly the eigenvector for the bifurcating solution. Approximate values of the critical Reynolds number (≈ 50) and Strouhal number, or non-dimensional frequency (≈ 0.14) for flow past a circular cylinder are known from experiment (Berger & Wille 1972; Coutanceau & Bouard 1977 a, b; Friehe 1980; Gaster 1971; Gerrard 1978; Hussain & Ramjee 1976; Kovasznay 1949; Mathis, Provansal & Boyer 1984; Nishioka & Sato 1974, 1978; Perry, Chong & Lim 1982; Roshko 1954; Tritton 1959, 1971; Zdravkovich 1969). The required initial guess for this flow was obtained by calculating first the basic flow at $Re = 50$, and then identifying the complex eigenvalue nearest to $0 + 0.1i$ together with the corresponding eigenvector. The Hopf algorithm converged rapidly from this initial guess.

We then altered the aspect ratio Γ of the computational domain, and by this means produced elliptical bodies with a range of eccentricities; estimates Re_c^{est} and St_c^{est} were obtained by parameter stepping the Hopf algorithm. These values are of course results calculated with a distorted computational domain,

$$-5\Gamma \leqslant x \leqslant 15\Gamma, \quad -5 \leqslant y \leqslant 5, \tag{35}$$

so the basic flow at $Re = Re_c^{\text{est}}$, the complex eigenvalue nearest to $0 + i\,St_c^{\text{est}}$, and the corresponding eigenvector were recalculated for a grid appropriate to each ellipse that covered the prescribed domain (33). These results provided the initial guess for the Hopf algorithm, which then converged rapidly in most cases. It did not converge for the more extreme eccentricities, for which it was necessary to start from an intermediate value of the eccentricity at which the Hopf point had already been found. In this way the Hopf point was obtained for ellipses with an eccentricity in the range 10^{-4} to 2.5. The ellipse of eccentricity 10^{-4} is of course effectively a flat plate.

Initial guesses for the rotated ellipse and flat plate were then obtained by extrapolation from the results for the unrotated ellipse and plate, on the assumption
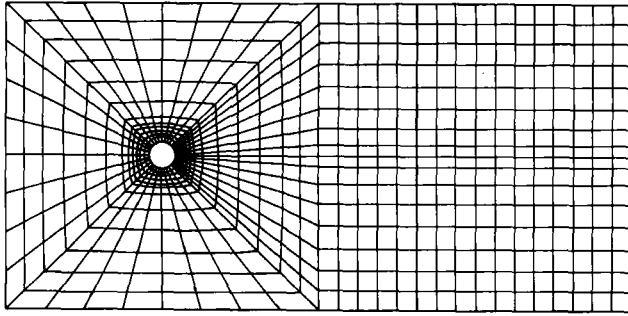
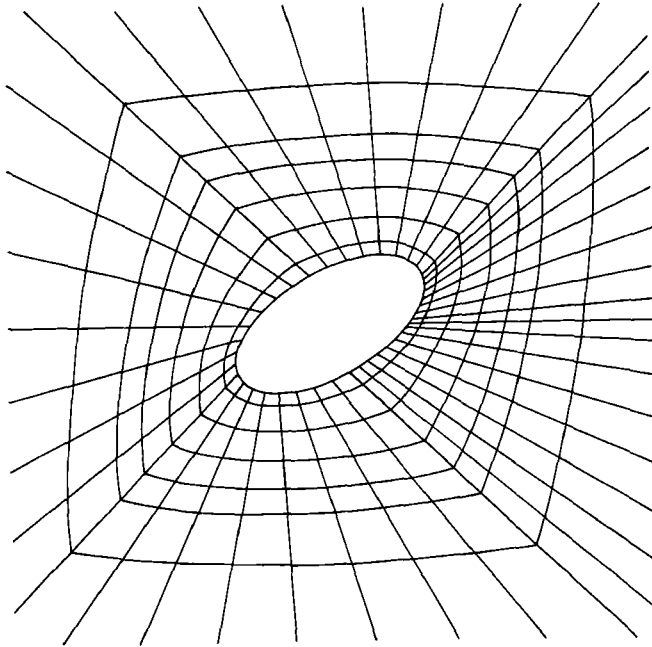FIGURE 4. Finite-element grid for simulating flow past a circular cylinder.

FIGURE 5. Detail of the grid for simulating flow past an ellipse with major axis 1.0 and minor axis 0.5, oriented at an angle of 60° to the flow.

that the Hopf point is essentially determined by the area of the body presented to the flow, that is that the Hopf point is determined by Re^D only. The results show that although this assumption provides a good initial guess at small rotations, it becomes progressively poorer as the rotation is increased. For the isosceles triangle appropriate initial guesses were obtained by a combination of extrapolation from results for the flat plate and parameter stepping.

Although this procedure sounds quite complicated, it was straightforward in practice once the Hopf point for the circular cylinder had been found. Our experience emphasizes the great advantage of determining an initial guess by parameter stepping from some related problem for which the Hopf point is already known.

In the original problem we were fortunate that experiment had already indicated the position of the Hopf point for the circular cylinder. If this result had not been available, it would have been necessary to search laboriously for potential Hopf

		Coarse grid (8320 Freedoms)	Fine grid (32 832 Freedoms)
Flow calculation	Assemble matrix	3.5	11.0
	Assemble right-hand side		
	LU decomposition and forward elimination	3.2	31.4
	Back substitution	0.1	0.5
Eigenvalue calculation	Assemble extended matrix	4.0	11.0
	Assemble extended right-hand side	2.4	8.3
	LU decomposition of extended matrix and forward elimination	16.0	213.4
	Back substitution	0.3	1.5
Hopf algorithm	Assemble matrix	2.8	11.0
	Assemble right-hand sides		
	LU decomposition and forward elimination	3.4	31.4
	Back substitution	0.2	0.9
	Assemble extended matrix	8.8	35.3
	Assemble extended right-hand side		
	LU decomposition of extended matrix and forward elimination	16.0	213.4
	Back substitution	0.3	1.5

TABLE 1. Computational times (s) for the various matrix operations for the coarse and fine grids

points by first choosing Reynolds numbers, and then for each Reynolds number scanning the neighbourhood of the imaginary axis for complex eigenvalues; once an eigenvalue with negative real part has been found, it is simple to locate the corresponding Hopf bifurcation. However, the search for complex eigenvalues is easy to automate. This automatic scanning was used to search for potential 'resonances' of the Hopf eigenvalue for flow past the cylinder. None were found in the range $0 < St < 10$.

3.3. *Computational costs*

It is worth adding a note on computational costs. The cost of determining Re_c and St_c for a particular problem depends upon whether it is possible to use the Hopf algorithm alone, starting from a good initial guess, or whether it is necessary to calculate first the flow, then an eigenvalue, and then use the Hopf algorithm; and of course the cost depends upon the number of iterations at each stage.

Each iteration of the flow calculation has five steps: assemble the matrix g_x, assemble the right-hand side g, an *LU* decomposition, a forward elimination, and a back substitution. Typically four or five iterations suffice for convergence to eight or more significant figures.

The cost of the eigenvalue calculation depends upon the chosen algorithm. For example, complex inverse iteration with no update of the eigenvalue requires the reckoning of only a single extended matrix, and hence only one *LU* decomposition; each iteration involves only assembling an extended right-hand side, a forward elimination, and a back substitution. Typically five to twenty iterations provide an eigenvalue and associated eigenvector sufficient for a good initial guess for the Hopf algorithm, provided that the initial guess for the frequency was adequate.

Axis parallel to flow $a_\parallel$	Re_c	St_c	Comment
10^{-4}	27.767	0.12368	Flat plate
0.1	29.680	0.12679	
0.3	32.765	0.13085	
0.5	35.704	0.13321	
0.8	40.990	0.13514	
0.9	43.100	0.13568	
1.0	45.403	0.13626	Circular cylinder
1.2	50.586	0.13766	
1.4	56.478	0.13943	
2.0	76.794	0.14644	

TABLE 2. Critical Reynolds number and corresponding Strouhal number for a range of ellipses oriented along the flow. The axis perpendicular to the flow has non-dimensional length 1. The axis parallel to the flow has length $a_\parallel$.

The first five steps in one Newton–Raphson iteration of the Hopf algorithm are: assemble the matrix g_X, assemble the appropriate two right-hand sides, *LU* decomposition of the matrix g_X, forward elimination, and back substitution. The additional steps involve the same procedure but with the matrix A^* for the system of equations (30). Typically four or five iterations of the Hopf algorithm gave convergence to eight significant figures or better.

The dominant costs in these operations are incurred in the matrix assembly and the *LU* decomposition. Table 1 collects representative CPU (Central Processor Unit) times for a CRAY1 carrying out calculations with the coarse and fine grids. The solver, which uses a very fast frontal method that we have developed, runs at speeds in excess of 100 MFLOPS (million floating point operations per second) for large problems. Some of the matrix operations are combined to increase efficiency, so some of the times given in table 1 are for more than one step. These times are only representative since the frontal solver performs partial pivoting which has some influence upon the speed of computation. Moreover, the times also depend upon the ordering of the elements; the chosen ordering gave acceptable times, although it was not optimal.

4. Results

Calculated values of critical Reynolds numbers and critical Strouhal numbers are collected in tables 2, 3, 5, 6 and 7 and illustrated in figures 6, 7, 8 and 9.

Table 2 contains St_c for ellipses oriented along the flow, and these results are plotted in figure 6. The dimension of the ellipse across the flow defines the unit of length (see figure 3a), and to this scale the dimension parallel to the flow has a length $a_\parallel$ ranging between 10^{-4} (corresponding to a flat plate) and 2. In particular for the circular body Re_c is 45.403 and St_c is 0.13626. The results from the fine grid are $Re_c = 46.136$ and $St_c = 0.13793$. It is believed that values of Re_c and St_c calculated by means of the Hopf algorithm using the chosen type of element converge at a rate proportional to the fourth power of the degree of refinement of the grid. Thus grid converged results $Re_c^{\text{converged}} = 46.184$ and $St_c^{\text{converged}} = 0.13804$ can be estimated. Calculations with significantly finer grids are not currently practicable.

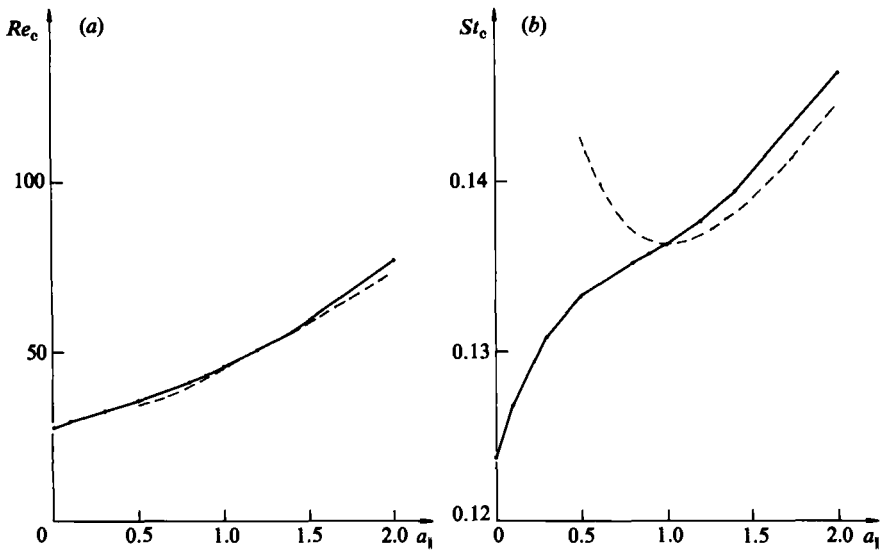Table 3 again gives Re_c and St_c for a range of ellipses aligned with the flow, but

FIGURE 6. Re_c and St_c for ellipses oriented along the flow: (a) Re_c, and (b) St_c. (Results obtained by parameter-stepping on Γ are shown dashed.)

Axis parallel to the flow $a_\parallel$	Re_c	St_c
0.5	34.847	0.14256
0.6	36.096	0.14028
0.7	37.957	0.13815
0.8	40.351	0.13695
0.9	42.862	0.13641
1.0	45.403	0.13626
1.2	50.693	0.13675
1.4	56.207	0.13808
1.6	61.724	0.13983
1.8	67.477	0.14190
2.0	73.427	0.14431

TABLE 3. Critical Reynolds number and corresponding Strouhal number for a range of ellipses oriented along the flow, obtained by parameter stepping on the aspect ratio so that the domain is stretched to be $-5\Gamma < x < 15\Gamma$ where Γ is the aspect ratio. Γ is of course equal to the axis of the ellipse along the flow

these results, which are shown by a dashed line in figure 6, were obtained with a computational domain (35) distorted so that the aspect ratio equals the eccentricity of the ellipse. These results could thus be obtained easily and relatively cheaply by parameter stepping from the results for the circular body. Thus a comparison of these results with those of table 2 illustrates the effect upon Re_c and St_c of varying the physical domain; such effects are of course most pronounced at extreme values of the aspect ratio. We expect that the results of table 3 will become progressively more inaccurate as Γ is decreased because the computational domain is ultimately too small to contain a complete eddy behind the body. However, the major purpose of these results was to serve as initial guesses for calculations on the standard domain (33) and they fulfilled this purpose well.

Re_c	Re	St	Author	Comment
45.403	45.403	0.13626 ⎫		⎧ Coarse grid
46.136	46.136	0.13793 ⎬	This study	⎨ Fine grid
46.184	46.184	0.13804 ⎭		⎩ Richardson extrapolation
—	100	0.16	Braza	Time-dependent calculation
—	50	0.12 ⎫	Roshko	Experiment
—	100	0.17 ⎭		
—	50	0.14 ⎫	Gresho	Time-dependent calculation
—	100	0.18 ⎭		
—	50	0.12 ⎫	Berger	Experiment
—	100	0.15 ⎭		
—	50	0.12 ⎫	Tritton	Experiment
—	100	0.16 ⎭		
—	50	0.12 ⎫	Freihe	Experiment
—	100	0.16 ⎭		
34–43	—	—	Coutanceau	Experiment
40	—	0.12	Kovasznay	Experiment
48	—	0.12	Nishioka & Sako	Experiment
47	—	—	Mathis et al.	Experiment

TABLE 4. Comparison of the results of this study for a circular cylinder with experimental results and time-dependent calculations. In most cases we present St values at several Re values greater than Re_c since Re_c was not obtained

Angle between minor axis and flow $\theta°$	Re_c	St_c
0	35.704	0.13321
10	36.392	0.13442
20	38.566	0.13817
30	42.611	0.14484
40	49.331	0.15511
50	60.169	0.17008
60	77.080	0.19106
70	101.27	0.21758
80	128.27	0.24386
85	137.86	0.25261
88	140.85	0.25528
90	141.44	0.25580

TABLE 5. Critical Reynolds numbers and corresponding Strouhal numbers for ellipses with major axis 1 and minor axis 0.5 oriented at various angles θ to the flow

Table 4 compares our results for the circular body with results from time-dependent calculations (Braza, Chassaing & Minh 1987; Fromm & Harlow 1969; Gresho et al. 1984; Thoman & Szewczyk 1969) and with measured values (Berger & Wille 1972; Coutanceau & Bouard 1977a, b; Friehe 1980; Gaster 1971; Gerrard 1978; Hussain & Ramjee 1976; Kovasznay 1949; Mathis et al. 1984; Nishioka & Sato 1974, 1978; Perry et al. 1982; Roshko 1954; Tritton 1959, 1971; Zdravkovich 1969). In general these experiments or time-dependent calculations were carried out at a Reynolds
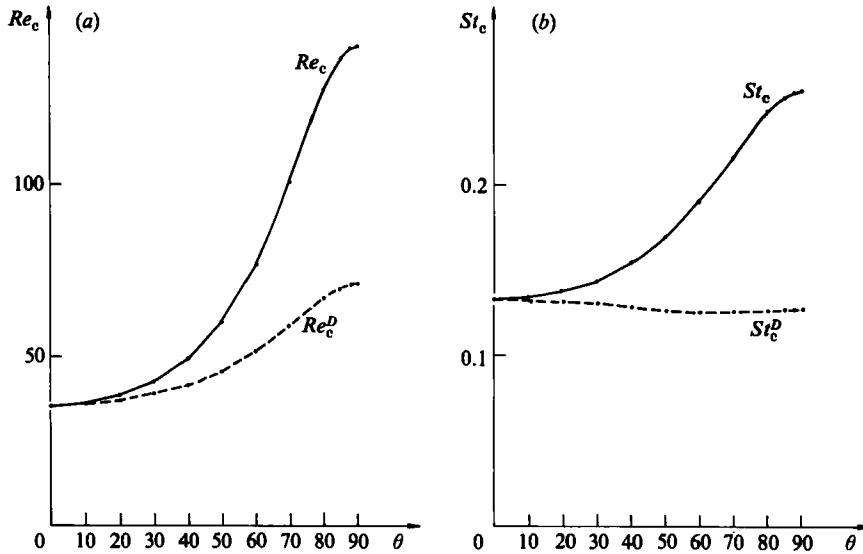
FIGURE 7. Re_c and St_c for ellipses with major axis 1.0 and minor axis 0.5, with minor axis at various angles to the flow: (a) Re_c and Re_c^D, and (b) St_c and St_c^D (Re_c^D and St_c^D are based on the cross-section D presented to the flow, and are shown dashed)

Angle $\theta°$	Re_c	St_c
0	27.767	0.123 68
10	28.153	0.124 49
20	29.952	0.128 91
30	32.785	0.135 24
40	39.931	0.150 67
50	52.926	0.175 96
60	87.883	0.224 07

TABLE 6. Critical Reynolds number and corresponding Strouhal number for a flat plate with its normal oriented at an angle θ to the flow

number greater than Re_c, which could not be determined precisely by either of these means, although there is general agreement that Re_c is about 40. We have therefore collected from the literature, where possible, values of St for several values of Re greater than Re_c. It should also be borne in mind that Re_c and St_c will be affected by the choice of domain and boundary conditions in time-dependent simulations, or by the experimental configuration. For example, Coutanceau & Bouard discuss how the size of the cylinder relative to the overall flow apparatus affects Re_c, which they find to vary between 34 and 43.

It should be noted that it is difficult to determine Re_c experimentally. In particular it is necessary to ensure that the residual turbulence in the inlet is reduced to a very low level as otherwise this can excite the periodic flow at Re below Re_c. Such residual turbulence is probably the reason for the slightly low values quoted by Coutanceau & Bouard. It should be noted that the calculated results agree very well indeed with the recent experimental results of Mathis *et al.* (1984) and Nishioka & Sato (1974, 1978).

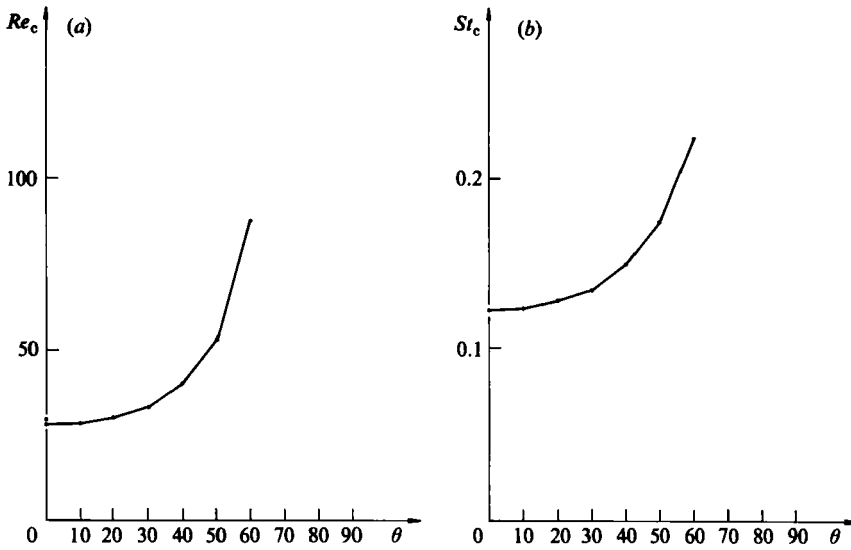Table 5 and figure 7 collect values of Re_c and St_c for ellipses with major axis 1 and

FIGURE 8. Re_c and St_c for a flat plate with its normal at various angles to the flow:
(a) Re_c, and (b) St_c.

Height h	Re_c	St_c	
(0)	(27.767)	(0.123 68)	(Flat plate result)
0.1	27.707	0.123 47	
0.3	29.270	0.126 92	
0.5	31.196	0.130 66	
0.8	34.318	0.135 54	
1.0	36.370	0.137 97	
1.2	38.343	0.139 78	
1.4	40.224	0.141 10	
2.0	45.324	0.143 24	

TABLE 7. Critical Reynolds number and corresponding Strouhal number for isosceles triangles oriented towards the flow with varying height h

minor axis 0.5, the minor axis being disposed at various angles to the flow (see figure 3b). Figure 6 also plots values of Re_c^D and St_c^D, which are based upon the cross-section D of the ellipse perpendicular to the flow rather than upon L_y. The results presented in this way show that to a large extent the critical Strouhal number only depends upon the perpendicular cross-section of the body although the critical Reynolds number reflects also the overall shape of the body.

In table 6 and figure 8 appear values of Re_c and St_c for flat plates (strictly for ellipses with minor axis 10^{-4}) which are oriented at various angles to the flow (see figure 3c). Re_c and St_c for various isosceles triangles are found in table 7 and figure 9. The base of each triangle is perpendicular to the flow and the apex points upstream (see figure 3d).

Figure 10 represents the flow X_c at the Hopf bifurcation, for flow past a circular body, and figures 11 and 12 the real and imaginary parts ξ_r and ξ_i of the bifurcating eigenvector. These figures show both the streamlines and the velocity vectors. The
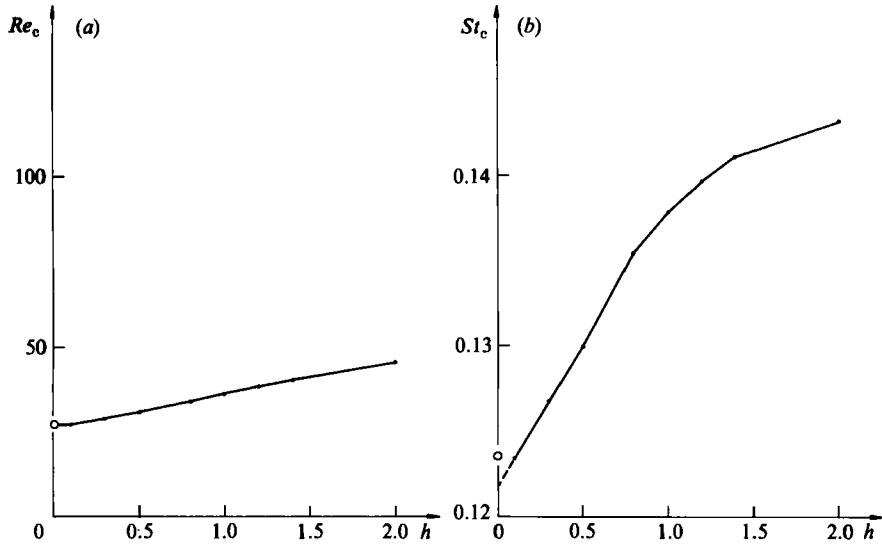
FIGURE 9. Re_c and St_c for various isosceles triangles that are oriented with their apices directed into the flow: (a) Re_c, and (b) St_c. o indicates flat plate result.
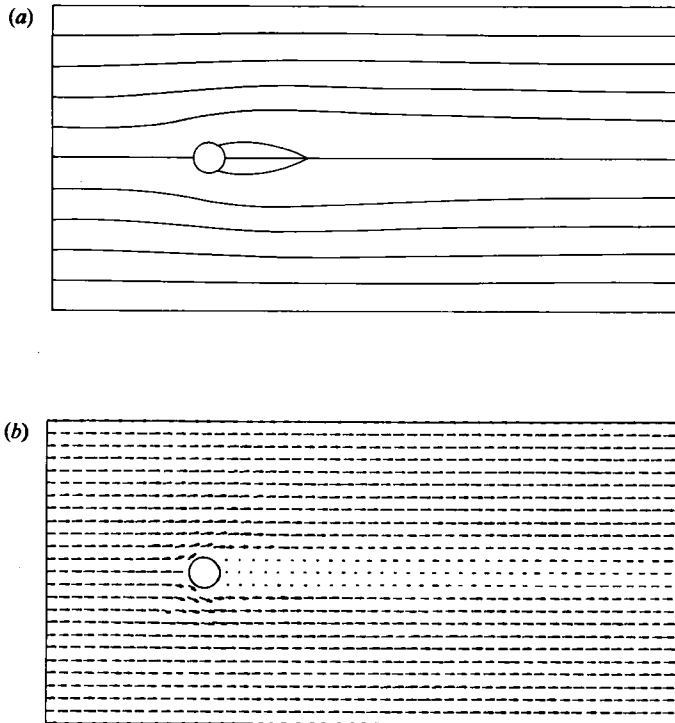

FIGURE 10. Streamlines and velocity vectors for flow X_c at the bifurcation marking the transition to oscillatory flow.
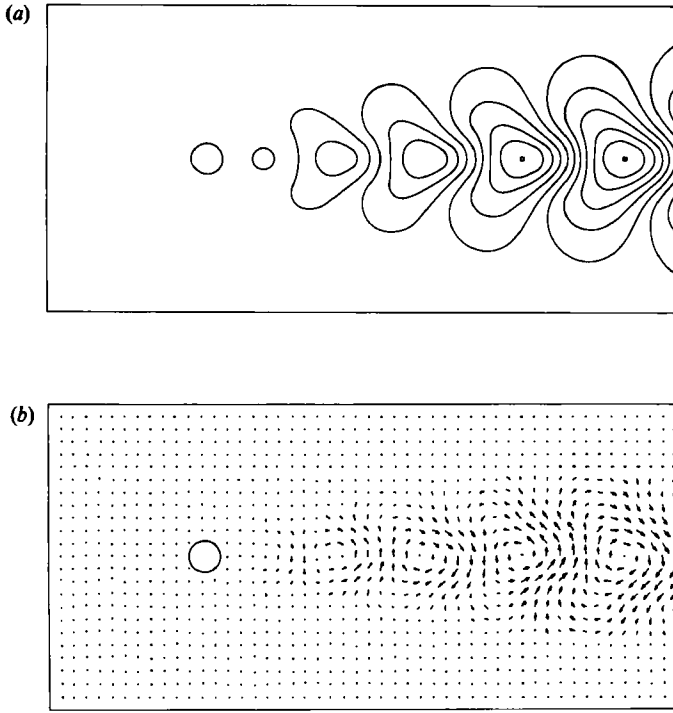
(*a*)

(*b*)

FIGURE 11. Streamlines and velocity vectors for the real part ξ_r of the bifurcating eigenvector.
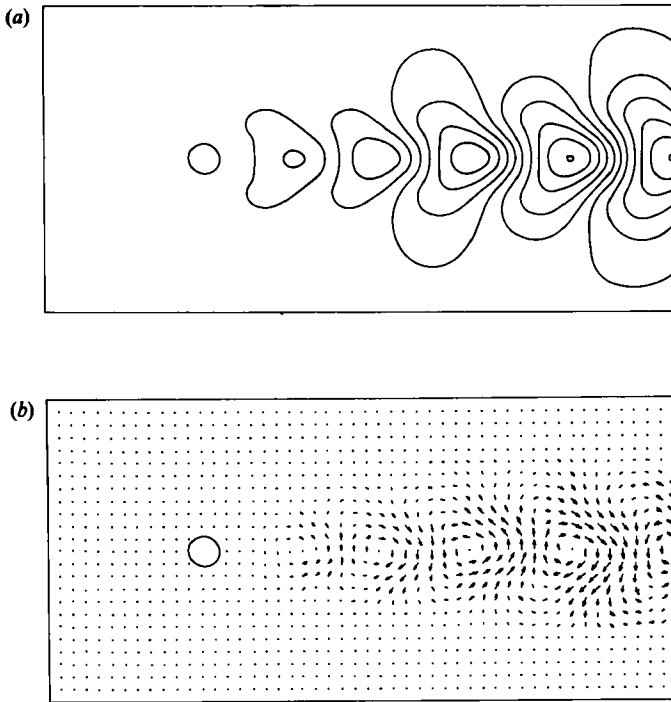
(*a*)

(*b*)

FIGURE 12. Streamlines and velocity vectors for the imaginary part ξ_i of the bifurcating eigenvector.
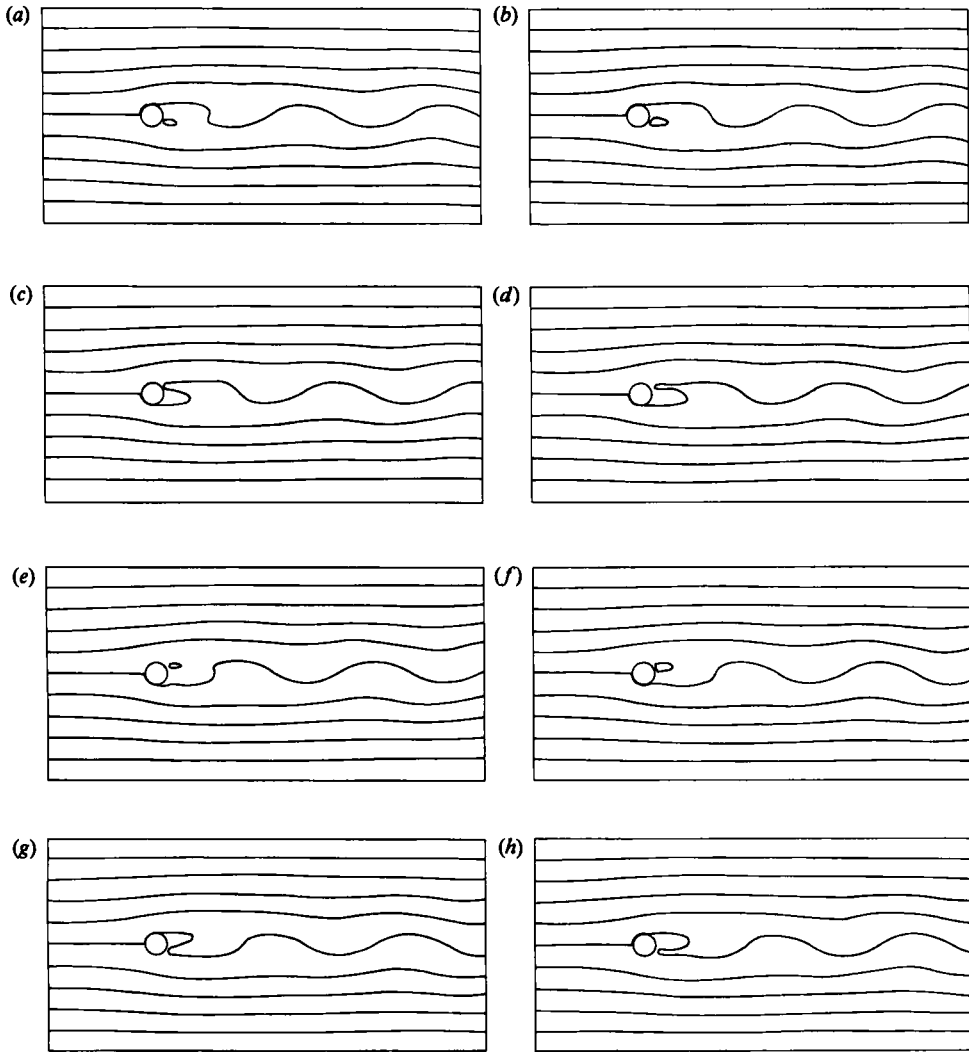
FIGURE 13. Snapshots of the instantaneous streamfunction, at intervals of $\frac{1}{8}$ the period of oscillation, for a flow at Re slightly greater than Re_c.

stream function ψ is obtained from the vorticity Ω by solving with finite elements the equation

$$-\nabla^2\psi = \Omega = \frac{\partial v}{\partial x} - \frac{\partial u}{\partial y}. \tag{36}$$

For values of Re slightly greater than Re_c the solution for the flow is of course of the form

$$X_c + a[\xi_r \cos(\omega t - \phi) - \xi_i \sin(\omega t - \phi)], \tag{37}$$

for some phase ϕ and small amplitude a, where $a = O((Re - Re_c)^{\frac{1}{2}})$. This is the theoretical behaviour expected near a Hopf bifurcation. Mathis *et al.* (1984) have confirmed experimentally that the amplitude behaves like $O((Re - Re_c)^{\frac{1}{2}})$. Figure 13 shows a sequence at intervals of $\frac{1}{8}$ of a period of oscillation of 'snapshots' of the instantaneous streamfunction derived by assuming $a = 0.2$ in (37). This approximates

the solution at some value of Re greater than Re_c that cannot be determined directly by the methods adopted in this study.

The flow X_c and the real and imaginary parts of the bifurcating eigenvector for the other body shapes have the same general behaviour as that illustrated for the circular cylinder.

5. Conclusions

The values of the critical Reynolds number Re_c for the onset of periodicity in flow past a cylindrical body, and the corresponding Strouhal number St_c or non-dimensional frequency, are in good agreement with the results of time-dependent calculations (Braza *et al.* 1987; Fromm & Harlow 1969; Gresho *et al.* 1984; Thoman & Szewczyk 1969) and experiment (Berger & Wille 1972; Coutanceau & Bouard 1977*a,b*: Friehe 1980; Gaster 1971; Gerrard 1978; Hussain & Ramjee 1976; Kovasznay 1949; Mathis *et al.* 1984; Nishioka & Sato 1974, 1978; Perry *et al.* 1982; Roshko 1954; Tritton 1959, 1971; Zdravkovich 1969), although neither time-dependent calculation nor experiment can give very accurate values for Re_c and St_c. The behaviour of Re_c and St_c as the body shape and orientation are varied are in accord with physical expectations.

The usefulness of the approach via extended systems is shown. It enables Re_c and St_c to be determined very accurately. It is also much cheaper than time-dependent calculations for determining these quantities. The approach using extended systems does not, of course, give directly the time-dependent behaviour at values of Re greater than Re_c, which can be obtained from time-dependent calculations. Thus extended systems and time-dependent calculations are to some extent complementary.

The use of extended system techniques also allows symmetries of the problem to be exploited in order to reduce the computational cost dramatically, which cannot be done in time-dependent calculations. In the case of flow past a circular cylinder for example, the steady flow is symmetric under reflections about the x-axis, while the bifurcating solution is antisymmetric. Both the calculation of the flow and the calculation of the Hopf bifurcation point can be carried out on the half grid $y > 0$, searching for a symmetric flow solution and antisymmetric bifurcating eigenvector. This reduces the cost by a factor of about eight.

One final comment that can be made is that the finite-element method is ideally suited to bifurcation studies. It is easy to modify a finite-element package to handle the extended systems; and of course the finite-element method is designed to handle complicated geometries as shown by the examples considered here.

In future work we intend to examine the onset of periodic behaviour in flow past bodies in unbounded domains, which can be treated in the same way as above, although more care is needed with the boundary conditions at infinity. We also intend to study the behaviour of the periodic solution beyond the Hopf point using extensions of these techniques.

REFERENCES

BATCHELOR, G. K. 1967 *An Introduction to Fluid Dynamics*. Cambridge University Press.

BERGER, E. & WILLE, R. 1972 Periodic flow phenomena. *Ann. Rev. Fluid Mech.* **4**, 313.

BRAZA, M., CHASSAING, P. & MINH, H. HA. 1987 A numerical study of the dynamics of different scale structures in the near wake of a circular cylinder in laminar to turbulent transition. In *Numerical Methods in Laminar and Turbulent Flow*. Pineridge (to appear.)

COUTANCEAU, M. & BOUARD, R. 1977*a* Experimental determination of the viscous flow in the wake of a circular cylinder in uniform translation. Part 1 Steady flow. *J. Fluid Mech.* **79**, 231.

COUTANCEAU, M. & BOUARD, R. 1977*b* Experimental determination of the viscous flow in the wake of a circular cylinder in uniform translation. Part 2 Unsteady flow. *J. Fluid Mech.* **79**, 257.

DYKE, M. VAN 1982 *An Album of Fluid Motion.* Parabolic Press.

FRIEHE, C. 1980 Vortex-shedding from cylinders at low Reynolds numbers. *J. Fluid Mech.* **100**, 237.

FROMM, J. E. & HARLOW, F. H. 1963 Numerical treatment of the problem of vortex street development. *Phys. Fluids* **6**, 975.

GASTER, M. 1971 Vortex-shedding from circular cylinders at low Reynolds numbers. *J. Fluid Mech.* **46**, 749.

GERRARD, J. 1978 The wakes of cylindrical bluff bodies at low Reynolds numbers. *Phil. Trans. R. Soc. Lond.* A **288**, 351.

GRESHO, P. M., CHAN, S. T., LEE, R. L. & UPSON, C. D. 1984 A modified finite-element method for solving the time-dependent incompressible Navier–Stokes equations. Part 2 Applications. *Intl J. Numer. Meth. Fluids* **4**, 619.

GRIEWANK, A. & REDDIEN, G. 1983 The calculation of Hopf points by a direct method. *IMA J. Numer. Anal.* **3**, 295.

HUSSAIN, A. K. M. F. & RAMJEE, V. 1976 Periodic wake behind a circular cylinder at low Reynolds number. *Aero Q.* **27**, 127.

JACKSON, C. P. 1982 The TGSL finite-element subroutine library. *Harwell Rep.* AERE-R.10713.

JEPSON, A. D. 1981 Numerical Hopf bifurcation. Thesis part 2, California Institute of Technology, Pasadena, CA USA.

KOVASZNAY, L. S. G. 1949 Hot-wire investigation of the wake behind cylinders at low Reynolds numbers. *Proc. R. Soc. Lond.* A **198**, 194.

MARSDEN, J. E. & MCCRACKEN, M. 1976 The Hopf bifurcation and its applications. Springer.

MATHIS, C., PROVANSAL, M. & BOYER, L. 1984 The Bénard–von Kármán instability: an experimental study near the threshold. *J. Phys. Lett. Paris* **45**, L483.

NISHIOKA, M. & SATO, H. 1974 Measurements of velocity distribution in the wake of a circular cylinder at low Reynolds numbers. *J. Fluid Mech.* **65**, 97.

NISHIOKA, M. & SATO, H. 1978 Mechanism of determination of the shedding frequency of vortices behind a cylinder at low Reynolds numbers. *J. Fluid Mech.* **89**, 49.

PERRY, A., CHONG, M. & LIM, T. 1982 The vortex shedding process behind two-dimensional bluff bodies. *J. Fluid Mech.* **116**, 77.

ROSHKO, A. 1954 On the development of turbulent wakes from vortex streets. *NACA Rep.* no. 1191.

THOMAN, D. A. & SZEWCZYK, A. A. 1969 Time-dependent viscous flow over a circular cylinder. *Phys. Fluids,* Supp. 2, p. 76.

TRITTON, D. J. 1959 Experiments on the flow past a circular cylinder at low Reynolds numbers. *J. Fluid Mech.* **6**, 547.

TRITTON, D. J. 1971 A note on vortex streets behind circular cylinders at low Reynolds numbers. *J. Fluid Mech.* **45**, 203.

TRITTON, D. J. 1977 *Physical Fluid Dynamics.* Van Nostrand Reinhold.

WILKINSON, J. H. 1965 *The Algebraic Eigenvalue Problem.* Oxford University Press.

ZDRAVKOVICH, M. 1969 Smoke observations of a Kármán vortex street. *J. Fluid Mech.* **37**, 491.